Chinese Chemical Letters 37 (2026) 111837

Contents lists available at ScienceDirect

Chinese Chemical Letters

journal homepage: www.elsevier.com/locate/cclet

HOF-based catalytic platform combining sonodynamic therapy and bioorthogonal activation of immunosuppression reversal for cancer therapy

Huanhui Wang, Longyi Nan, Yan Zheng*, Jianpeng Guo*, Guangchun Piao*

Key Laboratory of Natural Medicines of the Changbai Mountain, Ministry of Education, College of Pharmacy, Yanbian University, Yanji 133002, China

ARTICLE INFO

Article history:
Received 9 July 2025
Revised 11 September 2025
Accepted 12 September 2025
Available online 12 September 2025

Keywords:
Sonodynamic
Hydrogen-bonded organic frameworks
Bioorthogonal reaction
Immunogenic cell death
Immune evasion

ABSTRACT

The combination of sonodynamic therapy (SDT) and immunotherapy exhibits potent anticancer efficacy. However, most sonosensitizers produce reactive oxygen species (ROS) with low efficiency under ultrasound (US). Chemotherapy-induced immunogenic cell death (ICD) is also plagued by toxic side effects, suboptimal efficacy, and immune escape. Herein, we developed a cancer therapy platform based on a sonosensitizer, iron porphyrin (Fe(III) meso–tetra(4-carboxyphenyl)porphine chloride, FeTCPPCl), which self-assembles into a hydrogen-bonded organic framework (PHOF-1). This platform enables precise activation and spatiotemporal controlled release of prodrugs, thereby inducing ICD efficiently and safely. Specifically, PHOF-1 bioorthogonally activates the doxorubicin prodrug (pro-DOX) *in situ*, synergizing with sonodynamic immunotherapy. This strategy, which combines SDT with *in situ* prodrug activation, minimizes drug side effects and maximizes therapeutic effects. Additionally, this system activates the metformin (Glucophage) prodrug (pro-MET), with ATP depletion leading to upregulated adenosine monophosphate activated protein kinase (AMPK) expression, increased programmed death-ligand 1 (PD-L1) degradation, and reversal of tumor immunosuppression. Remarkably, SDT combined with bioorthogonal *in situ* immune activation represents a novel approach to enhance cancer immunotherapy. This synergy effectively converts "cold" tumors into "hot" tumors by promoting ICD and reducing PD-L1 expression, thereby improving immunotherapy efficacy. The integration of SDT and bioorthogonal chemistry offers a controllable therapeutic strategy with reduced immune-related adverse effects, providing a promising avenue for safer and more effective cancer immunotherapy through the induction of adaptive antitumor immunity.

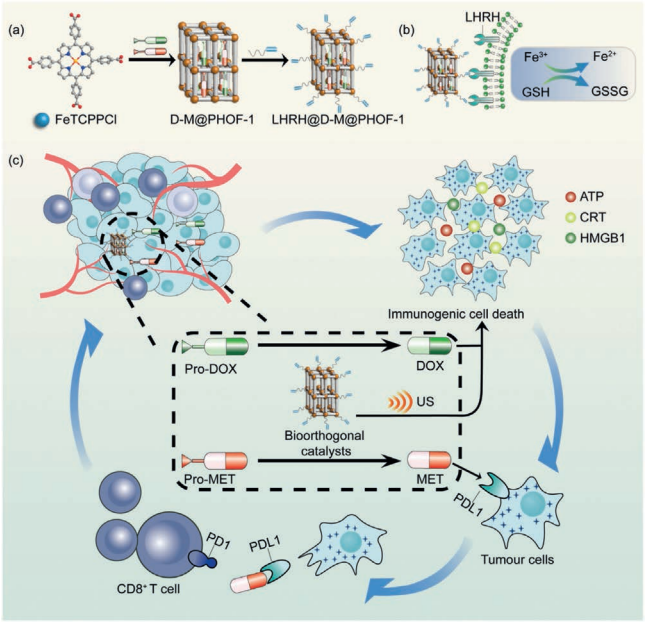
© 2026 Published by Elsevier B.V. on behalf of Chinese Chemical Society and Institute of Materia Medica, Chinese Academy of Medical Sciences.

Sonodynamic therapy (SDT), an emerging and notable US-based therapeutic approach for noninvasive cancer treatment, offers high tissue-penetrating capability, non-ionizing properties, high controllability, and low cost [1–3]. SDT produces sonoluminescence through the cavitation effect, activates the sonosensitizer to generate electrons, reacts with the surrounding oxygen (O_2) to generate cytotoxic singlet oxygen ($^1O_2$), and induces apoptosis of cancer cells [4]. However, sonosensitizers have low efficiency in generating reactive oxygen species (ROS) and cannot induce effective immunogenic cell death (ICD). In addition, T cell activity is suppressed due to the programmed death-ligand 1 (PD-L1) on the cell surface, contributing to an immunosuppressive tumor microenvironment [5]. These factors limit the clinical application of sonosensitizers. The development of drug delivery platforms with high ROS generation efficiency that can specifically trigger a strong immune response at tumor sites has become an urgent problem to be solved.

Chemotherapy, known for its ability to induce ICD and initiate a strong immune response, plays a dominant role in clinical trials [6–9]. SDT combined with the chemotherapeutic drug doxorubicin (DOX) could trigger a robust immune response by promoting ICD, showing great application potential [10–12]. Additionally, metformin (Glucophage) is used as a model drug to degrade PD-L1 and overcome the immune escape of triple-negative breast cancer (TNBC) [13–15]. However, toxic side effects in normal tissues caused by stochastic biodistribution of systemic administration hindered its development, which prompted us to synthesize prodrugs with bioorthogonal groups (aryl azide carbamate moieties), denoted as pro-DOX and pro-MET. Prodrugs, which carry chemical moieties that block certain essential parts of the parent drugs, have long been used to reduce serious adverse effects in cancer therapy.

* Corresponding authors.
E-mail addresses: zhengyan_0308@163.com (Y. Zheng), gjp807@ybu.edu.cn (J. Guo), gcpiao@ybu.edu.cn (G. Piao).

https://doi.org/10.1016/j.cclet.2025.111837
1001-8417/© 2026 Published by Elsevier B.V. on behalf of Chinese Chemical Society and Institute of Materia Medica, Chinese Academy of Medical Sciences.



Scheme 1. (a) Illustration of the synthesis of LHRH@D-M@PHOF-1. (b) Schematic diagram of the targeting mechanism of LHRH@D-M@PHOF-1 and the responsiveness of the tumor microenvironment. (c) Sonodynamic combined with immunotherapy strategy. LHRH, [D-Lys6] LHRH peptide; D, pro-DOX; M, pro-MET.

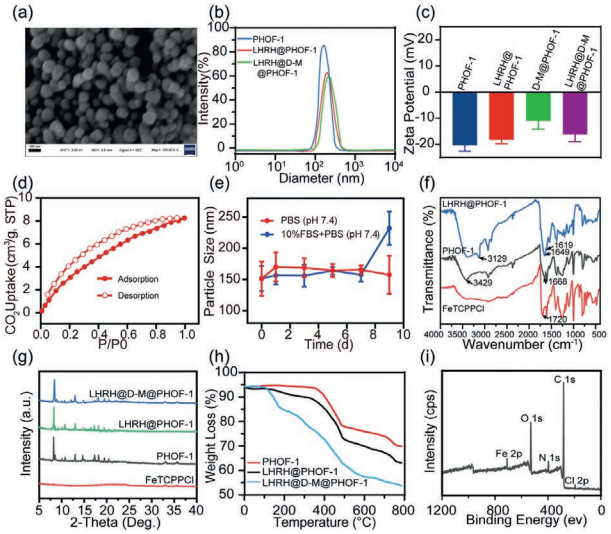


Fig. 1. (a) Scanning electron microscope (SEM) image of LHRH@D-M@PHOF-1. Scale bar: 1.0 μm. (b) Dynamic light scattering (DLS) curves of PHOF-1, LHRH@PHOF-1, LHRH@D-M@PHOF-1. (c) Zeta potentials of PHOF-1, LHRH@PHOF-1, D-M@PHOF-1, LHRH@D-M@PHOF-1. (d) BET curve of PHOF-1 nanoparticles. (e) LHRH@D-M@PHOF-1 remained stable for 7 days in a simulated physiological environment. (f) Fourier transform infrared spectroscopy (FTIR) spectra of FeTCPPCl, PHOF-1, LHRH@PHOF-1. (g) PXRD diffractograms of FeTCPPCl, PHOF-1, LHRH@PHOF-1, LHRH@D-M@PHOF-1. (h) Thermogravimetric analysis (TGA) spectrum for PHOF-1, LHRH@PHOF-1, LHRH@D-M@PHOF-1. (i) The XPS data of LHRH@D-M@PHOF-1. Data are shown as mean ± standard deviation (SD) ($n = 3$).

Bioorthogonal chemistry has been proven to be an effective method for *in situ* prodrug activation [16,17]. The bioorthogonal cleavage reaction is enjoying widespread attention in prodrug activation because it can liberate potent cytotoxic drugs under physiological conditions. Especially, the bioorthogonal cleavage reaction based on transition metal catalysts (TMCs) achieves site-specific targeted release while minimizing off-target toxicity. Hydrogen-bonded organic frameworks (HOFs) are frameworks assembled from organic units through hydrogen bonding interactions, including pure organic and metal-containing moieties TMCs. It has recently been found that iron porphyrins catalyze the reduction of azide to amino in the presence of glutathione (GSH). Iron porphyrin-based bioorthogonal catalysts can ensure tumor-selective bioorthogonal reactions triggered by overexpressed GSH in the tumor microenvironment. In addition, HOFs assembled from organic units by non-covalent interactions have shown excellent catalytic performance [18]. The extremely high surface area and uniform pore size distribution make them attractive platforms for transition metal catalysis of coupling reactions, CO_2 reduction, oxygen reduction, evolution reactions, *etc.* [19–22]. Therefore, if iron porphyrins are assembled into a HOF structure, the catalytic efficiency of the biological orthogonal reaction can be further improved.

Herein, we developed a nanoformulation that combines sonodynamic therapy with bioorthogonal prodrug activation, in which the sonosensitizer iron porphyrin (FeTCPPCl) forms a biocompatible HOF-based bioorthogonal pre-catalyst (PHOF-1). Meanwhile, pro-DOX and pro-MET are *in situ* encapsulated into PHOF-1, with peptide ligands modified on the surface for active targeting of breast cancer cells (Schemes 1a and b). Aptamer targeting and GSH-triggered decaging provide dual assurance for precise tumor-selective prodrug activation, preventing premature release and clearance (Scheme 1c). The HOF-based platform, combining SDT with bioorthogonal prodrug activation, offers a novel approach for precise and safe drug delivery. This strategy could have a profound impact on the safety and efficacy of tumor immunotherapy.

To implement a sonodynamic combined immunotherapy strategy, iron porphyrin HOFs, referred to as PHOF-1, were synthesized using the solvothermal method (Fig. S1 in Supporting information). Subsequently, pro-DOX and pro-MET were *in situ* encapsulated into PHOF-1 (namely D-M@PHOF-1). The synthetic routes and characterization data of pro-DOX and pro-MET are provided in Figs. S30 and S35–S40 (Supporting information). The LHRH aptamer was covalently grafted onto D-M@PHOF-1 *via* a 1-ethyl-3-(3-dimethylaminopropyl)carbodiimide reaction to prepare the final nanoparticulates (namely LHRH@D-M@PHOF-1). The coating amount of LHRH on D-M@PHOF-1 was calculated to be 1.154 nmol/mg by measuring the ultraviolet (UV) absorbance of the supernatant at $\lambda = 278$ nm (Fig. S2 in Supporting information). LHRH@D-M@PHOF-1 exhibited a uniform spherical morphology, and the particle size was found to be approximately 185 nm (Figs. 1a and b). The zeta potential of PHOF-1 is approximately −20.9 mV, which moderately increases to −11.2 mV after loading with the positively charged prodrug (Fig. 1c). This phenomenon indicates that the prodrug is successfully encapsulated into PHOF-1. Furthermore, the Brunauer-Emmett-Teller (BET) experiments confirmed that PHOF-1 possesses permanent porosity, making it an ideal candidate for a drug carrier (Fig. 1d). The stability of the nanoformulation is critical for *in vivo* transport and storage. Fig. 1e shows that the particle size of LHRH@D-M@PHOF-1 was stable for 7 days in a simulated physiological environment (10 % fetal bovine serum (FBS) at 37 °C).

LHRH ligands have the capability to actively recognize receptors on TNBC cells, so surface functionalization of PHOF-1 nanoparticles is fundamental for active targeting. As shown in Fig. 1f, the C=O stretching vibration of the free carboxylic acid located at 1720 cm^{-1} red-shifted to 1668 cm^{-1} after FeTCPPCl self-assembled into PHOF-1, and there is a broad and scattered peak at 3429 cm^{-1}, which illustrates the formation of intermolecular hydrogen bonds of carboxylic acid groups. The peaks at 3129, 1649, and 1620 cm^{-1} in LHRH@HOF are respectively the N–H stretching vibration of the amide bond, the C=O stretching vibration, and the N–H bend-

ing vibration, indicating that an amide reaction has occurred between -NH_2 on LHRH and -COOH on PHOF-1, which completes the surface functionalization. Powder X-ray diffraction (PXRD) characterized the structures of PHOF-1, D-M@PHOF-1 and LHRH@D-M@PHOF-1, indicating that the drug-loaded and surface-modified PHOF-1 retained its crystal structure (Fig. 1g). Thermogravimetric analysis results manifest that LHRH@D-M@PHOF-1 will decompose at around 120 °C (Fig. 1h), which is attributed to the decomposition of the prodrug. X-ray photoelectron spectroscopy (XPS) further verified the successful preparation of LHRH@D-M@PHOF-1 (Fig. 1i). Next, the drug loading capacity and drug release performance of LHRH@D-M@PHOF-1 were evaluated. To achieve a drug loading ratio close to 1:1, the drug loading capacity of both prodrugs in the supernatant was measured using UV–visible (UV–vis) spectroscopy. The results indicated that a concentration of 0.6 mg/mL is the optimal concentration for the simultaneous encapsulation of both prodrugs (Figs. S3 and S4 in Supporting information). The drug loading efficiency (LE) of PHOF-1 for pro-DOX and pro-MET was 22.3 % and 26.2 %, respectively, and the encapsulation efficiency (EE) was 73.9 % and 68.0 %, as determined by high-performance liquid chromatography (HPLC). The *in vitro* release profile of prodrug from PHOF-1 was evaluated by HPLC (Figs. S14c and d in Supporting information). As shown in Fig. S5 (Supporting information), LHRH@D-M@PHOF-1 is a pH-triggered drug release vehicle (pH 6.5). In particular, when it is exposed to US, the cumulative drug release is expanded from 40 % to 80 %. But in a normal physiological environment with pH 7.4, the two prodrugs released only 17.5 % (pro-DOX) and 18.2 % (pro-MET). These results indicate that LHRH@D-M@PHOF-1 exhibits good stability during circulation in body fluids.

The successful preparation of the PHOF-1 carrier platform prompted us to explore the performance of LHRH@PHOF-1 as a bioorthogonal pro-catalyst for azide reduction. In order to test the efficient catalytic reduction of the aryl azide to the corresponding amine in the presence of a biological mercaptan, a pre-fluorescent group based on fluorescein isothiocyanate (FITC) is employed. This pre-fluorescent group, called pro-FITC, encapsulates diazonium moieties to quench their fluorescence, thus determining catalytic efficiency. The synthetic route and characterization data of pro-FITC are provided in Figs. S30–S34 (Supporting information). First, we investigated the valence state of Fe in PHOF-1 after incubation with GSH. As shown in Fig. S6 (Supporting information), the XPS data revealed that the Fe binding energy of $2P_{1/2}$ decreased from 726.3 to 723.9, and the binding energy of $2P_{3/2}$ declined from 710.0 to 708.5. This shows that GSH reduces Fe^{3+} of PHOF-1 to Fe^{2+} (Fig. S6a). Under the influence of GSH, the UV absorption peak of FeTCPPCl red-shifted (Fig. S6b). Furthermore, the production of Fe^{2+} was confirmed with *o*-phenanthroline monohydrate (PHEN). As an iron ion probe, PHEN forms a red chelate with Fe^{2+}, which has a maximum absorption at 510 nm. The results in Fig. S6c exhibit that as the concentration of GSH increases, the level of Fe^{2+} gradually augments. These findings demonstrate that GSH possesses the capability to reduce Fe^{3+} within PHOF-1.

To evaluate the catalytic performance of LHRH@PHOF-1, the FITC precursor containing the same aryl azide blocking group as the prodrug (specifically pro-FITC) was employed as a model dye. As shown in Fig. S7 (Supporting information), the fluorescence of pro-FITC was significantly quenched (Fig. S7a). In a GSH-rich environment, the HOF-based Fe(III) catalyst (LHRH@PHOF-1) reacts with the azide to form the intermediate Fe(IV) azido complex, which is then converted to a reducing amine in the presence of a biothiol [23]. In the presence of LHRH@PHOF-1, GSH and Fe^{3+} respectively, no substantial fluorescence change of pro-FITC was detected due to the absence of Fe^{2+}. However, under the incubation of GSH + Fe^{3+} and Fe^{2+}, pro-FITC generated fluorescence (Fig. S7b). To confirm that Fe^{2+} produced by the reduction

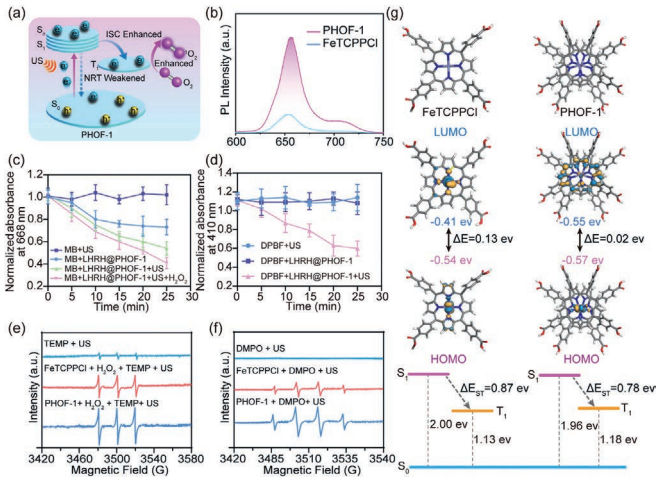


Fig. 2. (a) The proposed mechanism of $^1O_2$ generation by PHOF-1 under US irradiation. (b) The fluorescence spectrophotometer reveals the phosphorescence intensity of FeTCPPCl and PHOF-1. (c, d) Degradation of MB/DPBF by LHRH@PHOF-1 under different treatments. Data from three independent experiments are presented as mean ± SD ($n = 3$). (e, f) The ESR spectrum indicates the production of $^1O_2$ and $^{\bullet}OH$ in the US environment. (g) Schematic illustration of frontier molecular orbitals and energy gaps from TD-DFT calculations of FeTCPPCl and PHOF-1.

of GSH catalyzed the bioorthogonal reaction to release FITC, we observed that LHRH@PHOF-1 alone hardly triggers the degradation of the pro-FITC azide group (Fig. S7c). When Fe^{3+} and GSH are present concurrently, the fluorescence intensity progressively elevates as the incubation time increases (Fig. S7d). The identical phenomenon is observed in the presence of GSH+LHRH@PHOF-1 (Fig. S7e). Additionally, pro-FITC-coupled LHRH@PHOF-1 has fluoresced strongly in RAW264.7 cells when GSH is present (Fig. S8 in Supporting information). LHRH@PHOF-1 exhibited remarkable catalytic activity within living cells, suggesting that HOF-based biological orthogonal catalysts can effectively mitigate the adverse effects of complex living systems.

LHRH@PHOF-1 not only possesses the biological orthogonal catalysis capability but also has potential applications in SDT. PHOF-1 exhibits distinctive structural characteristics, such as the orderly arrangement of porphyrin units, spatial confinement, and optimal distances between porphyrin rings [24]. In the crystal structure of PHOF-1 (CCDC: 2231664), the distance between two porphyrin molecules is 3.5 Å, compared with 3.1 Å in non-crystalline FeTCPPCl molecules (Figs. S9a and b in Supporting information). These attributes significantly mitigate the aggregation-induced quenching (ACQ) effect resulting from π-π stacking and decrease the likelihood of internal and external conversion processes. Therefore, PHOF-1 reduces the non-radiative (NRT) decay pathway associated with thermal inactivation and intersystem crossing (ISC) processes, while improving the fluorescence emission efficiency and ROS generation ability (Fig. 2a). To elucidate the relationship between crystal structure and sonodynamic performance, we conducted a comparative analysis of the photoluminescence and ROS generation efficiencies of FeTCPPCl and PHOF-1. As depicted in Fig. 2b, in a 90 % aqueous solution, FeTCPPCl exhibited pronounced ACQ, leading to a substantially lower fluorescence intensity compared to PHOF-1.

To evaluate the sonodynamic performance of PHOF-1, we used methylene blue (MB) and 1,3-diphenylisobenzofuran (DPBF) as probes to detect $^{\bullet}OH$ and $^1O_2$ production, respectively (Figs. S10a and b in Supporting information). When a solution of MB containing PHOF-1 was exposed to US, the absorbance peak at 668 nm in the UV–vis spectrum decreased over time, indicating that the $^{\bullet}OH$ generated by US-triggered PHOF-1 oxidized MB into a colorless so-

lution. Furthermore, the addition of H_2O_2 resulted in a substantial generation of ·OH, which considerably reduces the peak intensity (Fig. 2c). Subsequently, the solution containing DPBF and PHOF-1 was exposed to a US trigger to detect $^1O_2$ production. As the US exposure time increased, the absorption peak of DPBF at 410 nm in the UV–vis spectrum gradually decreases, suggesting that the $^1O_2$ generated by US-triggered PHOF-1 oxidizes DPBF to colorless 1,2-dibenzoylbenzene over time. In contrast, negligible DPBF degradation was observed in the control group including the US group and the PHOF-1 only group (Fig. 2d). The generation of ·OH and $^1O_2$ was also detected using electron spin resonance (ESR) (Figs. 2e and f). 5,5-Dimethyl-1-pyrroline-*N*-oxide (DMPO) and 2,2,6,6-tetramethylpiperidine (TEMP) were employed as capture agents to measure ·OH and $^1O_2$, respectively. After FeTCPPCl was prepared into PHOF-1, there was an enhancement in the capacity for ROS production.

To further investigate the triplet energy transfer processes and the enhancement mechanism of ROS generation in PHOF-1, we conducted theoretical calculations on the optimized structures of FeTCPPCl and PHOF-1 using time-dependent density functional theory (TD-DFT). The highest occupied molecular orbital (HOMO) and the lowest unoccupied molecular orbital (LUMO) of FeTCPPCl are predominantly localized on the d orbitals of the Fe atom, exhibiting a substantial band gap of 0.13 eV. In contrast, within the PHOF-1 crystal structure, the HOMO remains on the d orbital of the Fe atom, whereas the LUMO is delocalized across the porphyrin moiety, leading to a reduced band gap of 0.02 eV (Fig. 2g). Additionally, the energy gaps between the first triplet state (T_1) and the singlet ground state (S_0) for FeTCPPCl and PHOF-1 were determined to be 1.13 and 1.18 eV, respectively. These values are significantly higher than the oxygen sensitization threshold of 0.98 eV required for the energy transfer from O_2 to $^1O_2$, indicating that both FeTCPPCl and PHOF-1 are capable of generating $^1O_2$ *via* an energy transfer mechanism. However, the ΔE_{ST} value of PHOF-1, which represents the energy gap between S_1 and T_1, was calculated to be 0.78 eV, substantially lower than the 0.87 eV of FeTCPPCl. This reduced ΔE_{ST} facilitates the ISC kinetics and enhances the $^1O_2$ generation capability of PHOF-1, corroborating the findings from ROS probe and ESR measurements. The intracellular ROS generation ability of LHRH@PHOF-1 was assessed using 2′,7′-dichlorofluorescin diacetates (DCFHDA), which undergoes rapid oxidation by ROS, emitting green fluorescence. Figs. S11 and S12 (Supporting information) illustrate that LHRH@PHOF-1 nanoparticles, under US irradiation (1.0 MHz, 0.58 W/cm^2, 2 min, 50 % duty), produce more ROS than FeTCPPCl and PHOF-1, indicating that more PHOF-1 nanoparticles are aggregated into 4T1 cells by active targeting. The LHRH@D-M@PHOF-1 group exhibited higher fluorescence intensity than the LHRH@PHOF-1 group, manifesting that DOX activated by PHOF-1 induces the production of sufficient intracellular ROS to mediate ICD.

As an active targeting agent, we quantified the cellular uptake of PHOF-1 nanoparticles using confocal laser scanning microscopy (CLSM). As shown in Figs. S13 and S14 (Supporting information), the FITC-LHRH@D-M@PHOF-1 group exhibited strong fluorescence within 4T1 mouse breast cancer cells (Fig. S13a). The flow cytometry data demonstrated comparable outcomes (Fig. S13b). Moreover, the 3-(4,5-dimethylthiazol-2-yl)-2,5-diphenyltetrazolium bromide (MTT) cytotoxicity assay demonstrated that PHOF-1 was non-cytotoxic across a broad range of concentrations from 20 μg/mL to 100 μg/mL (Fig. S13c). The aryl azide carbamate moiety of pro-DOX prevents its binding to deoxyribonucleic acid (DNA) and enzyme-mediated DNA damage to reduce its cytotoxicity. As displayed in Fig. S13d, the half maximal inhibitory concentration (IC_{50}) value of the free DOX was 0.7541 μmol/L, while this value was remarkably augmented ($P < 0.001$) in pro-DOX to be 8.530 μmol/L. Compared to pro-DOX, free DOX exhibits extraordinary cytotoxicity. Subsequently, pro-MET and pro-DOX were loaded into LHRH@PHOF-1 at a ratio of 1:1, and cell viability was detected to evaluate the activation of prodrugs by LHRH@PHOF-1 (Figs. S13e, S14a and b). After 3 h of treatment with GSH and LHRH@PHOF-1, HPLC analysis showed that the conversion rate of pro-DOX to DOX was 83.7 %, and the conversion rate of pro-MET to MET was 92.4 % (Figs. S14c and d). Mass spectrometry revealed the presence of transformed DOX and MET in 4T1 cell lysates. These data suggest that LHRH@PHOF-1 catalyzes the conversion of the prodrugs into DOX and MET within 4T1 cells through *in situ* bioorthogonal activation (Fig. S14e).

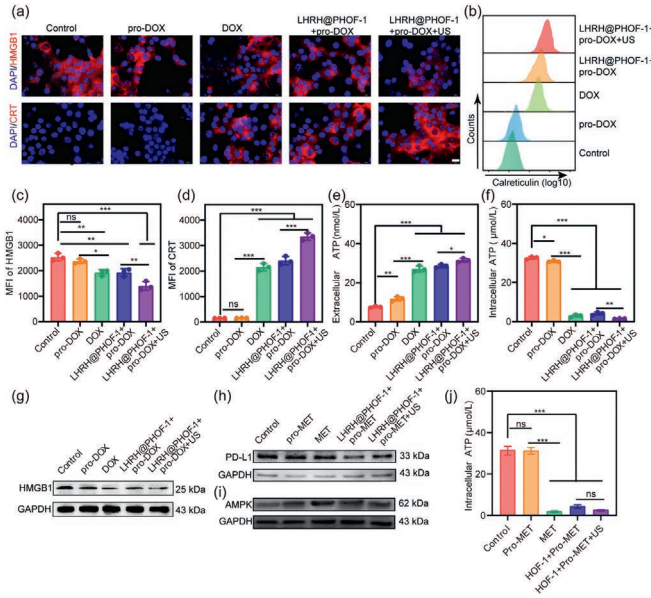


Fig. 3. (a) Immunofluorescence staining of CRT and HMGB1 after different treatments. Nuclei were stained with 4′,6-diamidino-2-phenylindole (DAPI, blue). Scale bar: 50 μm. (b) Quantification of CRT exposure on the surface of 4T1 cells by flow cytometry. Image J software calculated the MFI of HMGB1 (c) and CRT (d). Extracellular (e) and intracellular (f) ATP levels in 4T1 cells after different treatments. Western blot analysis evaluated the protein expression of HMGB1 (g), PD-L1 (h) and AMPK (i) under different conditions. (j) ELISA kit was used to measure intracellular ATP levels after different treatments. Data are presented as mean ± SD ($n = 3$). GAPDH, glyceraldehyde-3-phosphate dehydrogenase. ns, not significant. $^*P < 0.05$, $^{**}P < 0.01$, $^{***}P < 0.001$.

DOX is a representative anthracycline chemotherapy drug that enhances ICD caused by SDT [25]. The extracellular release of high-mobility group box 1 (HMGB1), adenosine triphosphate (ATP), and the exposure of calreticulin (CRT) on the cell surface represent three crucial signals of ICD [26]. Immunofluorescence assay showed that, compared with other groups, the expression level of HMGB1 in the LHRH@PHOF-1+pro-DOX+US group was substantially reduced (Fig. 3a). Western blot experiments consistently confirmed the above results, indicating that HMGB1 was released in large amounts into the extracellular environment (Fig. 3g). The extent of CRT exposure further revealed the ability of PHOF-1 to induce ICD. As depicted in Fig. 3a, intense red fluorescence was evident in both the LHRH@PHOF-1+pro-DOX group and the LHRH@PHOF-1+pro-DOX+US group, affirming the translocation of CRT to the 4T1 cell membrane. Furthermore, flow cytometry provided additional confirmation of CRT exposure across various groups (Fig. 3b). Utilizing ImageJ software to calculate the mean fluorescence intensity (MFI), the fluorescence intensity of CRT in the LHRH@PHOF-1+pro-DOX+US group was found to be 22 times higher than that in the pro-DOX group, while the fluorescence intensity of HMGB1 was observed to be 45.92 % lower (Figs. 3c and d). Regarding ATP secretion, extracellular ATP levels in the LHRH@PHOF-1 group exposed to US were measured to

be 3 times higher than those in the pro-DOX group. In contrast, intracellular ATP declined by 95.08 % (Figs. 3e and f). These results affirmed that pro-DOX activation by LHRH@PHOF-1 effectively triggered ICD. However, tumor cells usually overexpress the PD-L1 protein, which binds to the programmed cell death protein 1 (PD-1) receptor to inhibit the cytotoxic T lymphocyte (CTL). PD-L1 is also expressed on the surface of tumor cells, some of which have found ways to upregulate PD-L1 expression, leading to suppression of the host immune response, thereby producing tumor resistance. MET induces mitochondrial dysfunction, which causes ATP depletion. The consequent low-ATP stress condition promotes AMPK expression and accelerates PD-L1 degradation in tumor cells [27,28]. Intracellular ATP levels in 4T1 cells were quantified by enzyme-linked immunosorbent assay (ELISA) under different treatments. MET administration resulted in a 10-fold decrease in ATP levels relative to the control group (Fig. 3j). As displayed in Figs. 3h and i, MET activation by PHOF-1 (in the LHRH@PHOF-1+pro-MET and LHRH@PHOF-1+pro-MET+US groups) upregulated AMPK expression, resulting in PD-L1 degradation, blockade of the PD-1/PD-L1 axis, and prevention of drug resistance in 4T1 cells.

In oncology research, cell migration and aggression are key processes in TNBC metastasis and invasive growth, which habitually culminate in TNBC recurrence and treatment failure [29]. The effects of LHRH@D-M@PHOF-1 on the migration and invasion of 4T1 cells were investigated by scratch and transwell assays. Cell scratch assays are displayed in Fig. S15a (Supporting information). In the absence of US, the phosphate-buffered saline (PBS), FeTCPPCl, and LHRH@PHOF-1 groups showed significant proliferation of 4T1 cells in the scratch area after 24 h. However, under the influence of US, the LHRH@PHOF-1 and LHRH@PHOF-1+DOX/MET groups exhibited significantly fewer cells in the scratch area. Notably, the area recovery rate of the LHRH@D-M@PHOF-1 group was reduced by 96.9 % compared to the PBS group (Fig. S15b in Supporting information). In addition, the transwell assays illustrated that cell invasion of the LHRH@D-M@PHOF-1 group was significantly inhibited, especially after US exposure, and its cell number was reduced by 23 times compared with the PBS group (Fig. S16 in Supporting information). In conclusion, LHRH@D-M@PHOF-1 nanoformulation, triggered by US (1.0 MHz, 0.58 W/cm^2, 2 min, 50 % duty cycle), could effectively block the migration and invasion processes of 4T1 cells. The excellent results of *in vitro* experiments encourage us to further investigate the sonodynamic and catalytic bioorthogonal reaction mediated by LHRH@D-M@PHOF-1 nanosystems for the treatment of *in vivo* tumors.

In order to ensure the safe biological applications of PHOF-1, comprehensive *in vivo* toxicological studies of the nanoparticles were performed. The hemolysis rate of PHOF-1 was determined, and Fig. S17 (Supporting information) presents that the hemolysis rate of nanoparticles from 40 μg/mL to 100 μg/mL is <1 %, which implies that PHOF-1 nanoparticles could be administered intravenously. Subsequently, the major organs of mice were assessed using hematoxylin and eosin (H&E) staining, and body weight trends were monitored to assess the short- and long-term toxicity of the PHOF-1 nanoparticles. The tissue slices from mice injected with PHOF-1 appeared normal compared to those from mice not injected (Fig. S18 in Supporting information). As depicted in Fig. S19 (Supporting information), there was no notable change in the body weight of the mice, providing additional confirmation of the biological safety of LHRH@PHOF-1. The circulation rate and biodistribution were visualized using FITC-labeled LHRH@PHOF-1 (FITC-LHRH@PHOF-1). The pharmacokinetics of FITC-LHRH@PHOF-1 nanoparticles were consistent with a two-compartment model, with a half-life of 2.12 h (Fig. S20 in Supporting information). Following intravenous (i.v.) injection of FITC-LHRH@PHOF-1, the tumor-bearing mice were sacrificed, and the main organs and tumors were collected for *ex vivo* fluorescence

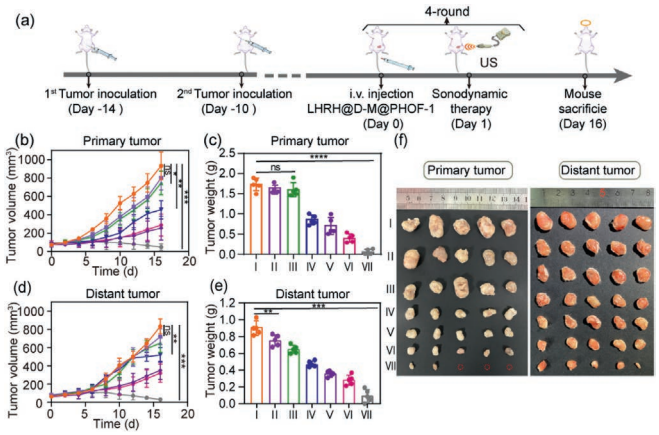


Fig. 4. (a) Schematic diagram of *in vivo* antitumor experiment protocol. Primary (b) and distant (d) tumor growth curves of 4T1 tumor-bearing mice under different treatments. Primary (c) and distant (e) tumor weight in different groups after 16 days of treatment. (f) Photographs of dissected primary tumors and distant tumors after various treatments. Data are presented as mean ± SD ($n = 5$). $^{*}P < 0.05$, $^{**}P < 0.01$, $^{***}P < 0.001$, $^{****}P < 0.0001$.

imaging. Fig. S21 (Supporting information) demonstrates that mice treated with LHRH@PHOF-1 nanoparticles for 24 h exhibited intense fluorescence compared to mice injected with PHOF-1. The inductively coupled plasma mass spectrometry (ICP-MS) results showed that LHRH@PHOF-1 effectively accumulated in the tumor site, which could be ascribed to the targeting capability and retention effect of the LHRH moiety (Fig. S22 in Supporting information).

Next, we assessed the antitumor effect of the PHOF-1-mediated SDT and bioorthogonal reaction in dual-tumor mice. All procedures were conducted in accordance with the National Institutes of Health Guide for the Care and Use of Laboratory Animals and were approved by the Animal Ethics Committee of Yanbian University (approval No. YD20240033). To establish a dual-tumor mice model of breast cancer, 4T1 cells at a density of 1×10^4 were injected into the right mammary fat pad and the upper limb region of BALB/c mice to generate primary and distant tumors, respectively, with an inoculation interval of 4 days (Fig. 4a). After 14 days, dual-tumor mice were obtained and randomly divided into 7 groups (I, PBS; II, LHRH@PHOF-1; III, pro-DOX+pro-MET; IV, PHOF-1+US; V, DOX+MET; VI, LHRH@D-M@PHOF-1; VII, LHRH@D-M@PHOF-1+US). To validate the capacity of LHRH@PHOF-1 to target tumors, we conducted imaging studies using 4T1 tumor-bearing BALB/c mice. The *in vivo* fluorescence imaging was performed at different time points after intravenous injection. As depicted in Fig. S23 (Supporting information), 6 h after injection, the fluorescence of LHRH@D-M@PHOF-1 was observed on the tumor, and the signal continued to intensify (groups VI and VII). Bioorthogonal pre-catalysts with targeted and sonodynamic properties maximize the effectiveness of immunotherapy while minimizing side effects. Additionally, the fluorescence intensity at the tumor site continued to increase sharply 24 h after intravenous injection. Therefore, the optimal time point for US treatment is 24 h after intravenous injection. As displayed in Figs. 4b and c, after 16 days of treatment, the primary tumor growth of group VII was significantly inhibited, while unobvious anti-cancer effect was observed in groups I, II, and III. The primary tumor growth curve revealed that tumors in BALB/c mice injected intraperitoneally with pro-DOX+pro-MET grew faster, indicating that pro-DOX and pro-MET had a weak inhibitory effect on tumor growth. Distinguished from group III, the primary tumor growth in group VII was markedly suppressed. The remarkable therapeutic effect was attributed to the enrichment of LHRH@PHOF-1 at the tumor site, which promoted the activation

of prodrug and the accumulation of ROS generated by the sonodynamic effect. The trend in distant tumor size change was consistent with that of primary tumors (Figs. 4d and e). At the observation endpoint, three mice in Group VII achieved complete elimination of primary tumors and exhibited effective suppression of distant tumors (Fig. 4f). Furthermore, mice experienced negligible fluctuations in body weight and changes in histological analysis of major organs after 16 days of various treatments (Figs. S24 and S25 in Supporting information). This indicates that LHRH@D-M@PHOF-1 combined with US therapy induces minimal side effects in mice.

Inspired by the admirable tumor suppressive effects, we explored the mechanisms of a bioorthogonally activated tumor immunosuppression reversal catalytic platform. The H&E results revealed aggravated necrosis in the tumor tissue of the LHRH@D-M@PHOF-1+US group, with significant cellular debris, whereas the dissected tumors in the PBS and pro-DOX + pro-MET groups showed no apparent apoptosis (Fig. S26 in Supporting information). The terminal deoxynucleotidyl transferase-mediated deoxyuridine triphosphate (dUTP) nick-end labeling (TUNEL) assays of tumor tissue further indicated that LHRH@D-M@PHOF-1+US could augment cancer cell apoptosis by reversing immunosuppression. HMGB1 and CRT were used as detection indicators to examine the activation of ICD. The immunohistochemistry and immunofluorescence results demonstrated strong HMGB1 release and enhanced CRT expression in the LHRH@D-M@PHOF-1+US treatment group. Fig. S26 shows that the PD-L1 level in the DOX+MET treated group was reduced compared with PHOF-1+US, indicating that MET inhibited the expression of PD-L1 and achieved the reversal of immunosuppression. These results confirm that LHRH@D-M@PHOF-1 actively targets the tumor site. The sonodynamic effect of PHOF-1 enhances chemotherapy-induced ICD, while activated MET reverses immune suppression, thus allowing continuous action of ICD.

For evaluation of the immune response elicited by the LHRH@D-M@PHOF-1 nanoformulation under US exposure, immune cells in the lymph nodes and tumor tissues, as well as serum cytokine levels, were analyzed after a 16-day treatment period. Single-cell suspensions were prepared for subsequent flow cytometric analysis (Fig. S27 in Supporting information) [30,31]. Mature dendritic cells (DCs) are the most potent antigen-presenting cells (APCs) and play a crucial role in the activation of naive T cells and the initiation of antitumor immune responses. Therefore, the maturation rate of DCs in lymph nodes was first evaluated. As shown in Fig. S28 (Supporting information), the DC maturation rate in the LHRH@D-M@PHOF-1+US group was significantly higher compared to the other groups (Figs. S28a and d). The proportion of mature DCs in this group reached 30.9%, which is 3 times higher than that of the blank formulation group (LHRH@PHOF-1). This is attributed to the specific activation of the adaptive immune response by LHRH@D-M@PHOF-1 nanoparticles under US conditions. MET enhances the cytotoxic activity of antigen-activated effector $CD8^+$ T cells against cancer cells by inhibiting PD-L1-mediated immunosuppressive signaling [27]. As shown in Figs. S28b and e, the proportion of $CD8^+$ T cells was 36.9% in the LHRH@D-M@PHOF-1+US group, 24.2% in the LHRH@D-M@PHOF-1 group, and 14.5% in the DOX+MET group, all markedly higher than in groups without MET treatment. Therefore, due to the maturation of DCs, infiltration of $CD4^+$ and $CD8^+$ T cells at tumor sites was most pronounced in mice treated with LHRH@D-M@PHOF-1 nanoparticles combined with US. In addition, the generation of memory T cells within tumor tissues (Figs. 28c and f) was enhanced, further indicating that mice treated with LHRH@D-M@PHOF-1+US developed immune memory and established long-term antitumor protection. Furthermore, under US conditions, the LHRH@D-M@PHOF-1 nanoplatform elicited the highest levels of cytokine secretion, including IFN-β, TNF-α, IL-6, IL-12, and IFN-γ, among all treatment groups (Figs. S28g–k). To evaluate the immune response within the tumor microenvironment, ELISA was used to quantify the levels of IFN-γ and granzyme B in tumor homogenates. Elevated cytokine concentrations in the treatment group suggest enhanced intra-tumoral T cell activation (Fig. S29 in Supporting information). This further confirms that LHRH@D-M@PHOF-1 promotes the recruitment and activation of immune cells, thereby converting “cold tumors” into “hot tumors” and eliciting a robust immune response.

In summary, we constructed a sonosensitive HOF-based bioorthogonal platform that delivers pro-DOX and pro-MET to induce ICD and reverse immune suppression. PHOF-1 modified with peptide LHRH is enriched at tumor sites through active targeting. In the presence of high levels of intratumoral GSH, FeTCPPCl is reduced to Fe^{2+}, triggering the bioorthogonal reaction. The activated pro-DOX and the SDT of PHOF-1 simultaneously induce ICD. Concurrently, the bioorthogonal reaction-generated MET, which inhibits PD-L1 expression and reversing immune suppression. Both *in vitro* and *in vivo* antitumor experiments demonstrate that the LHRH@D-M@PHOF-1 nanoformulation enables precise and safe drug delivery. This formulation not only shows satisfactory efficacy in antitumor therapy but also avoids dose-dependent side effects in normal organs and tissues. Furthermore, the bioorthogonal chemistry strategy has recently entered clinical trials (NCT04106492) [32], showing exciting potential for clinical translation. Given the satisfactory therapeutic effects of the designed strategy on the poorly immunogenic 4T1 mouse model, the sonodynamic effect and bioorthogonal reaction based on PHOF-1 offer great promise for safely and effectively enabling immunotherapy for various other types of cancer in clinical practice.

Declaration of competing interest

The authors declare that they have no known competing financial interests or personal relationships that could have appeared to influence the work reported in this paper.

CRediT authorship contribution statement

Huanhui Wang: Writing – original draft, Methodology, Investigation, Data curation. **Longyi Nan:** Visualization, Validation. **Yan Zheng:** Writing – review & editing, Conceptualization. **Jianpeng Guo:** Conceptualization. **Guangchun Piao:** Conceptualization.

Acknowledgments

This work was funded by the National Natural Science Foundation of China (No. 82460701), the Natural Science Foundation of Jilin Province, China (No. YDZJ202501ZYTS188).

Supplementary materials

Supplementary material associated with this article can be found, in the online version, at doi:10.1016/j.cclet.2025.111837.

References

[1] G. Lin, G.T. Nash, T. Luo, et al., Adv. Mater. 35 (2023) 2212069.
[2] Y. Zhang, J. Zhao, L. Zhang, et al., Nano Today 49 (2023) 101798.
[3] Y. Yang, J. Huang, M. Liu, et al., Adv. Sci. 10 (2023) 2204365.
[4] Q. Chen, M. Zhang, H. Huang, et al., Adv. Sci. 10 (2023) 2206244.
[5] X. Ren, Z. Cheng, J. He, et al., Nat. Commun. 14 (2023) 7021.
[6] G. Kroemer, L. Montégut, O. Kepp, et al., Nat. Rev. Immunol. 24 (2024) 912–928.
[7] B. Wu, B. Zhang, B. Li, et al., Signal Transduct. Target. Ther. 9 (2024) 274.
[8] Y. Chao, C. Liang, H. Tao, et al., Sci. Adv. 6 (2020) eaaz4204.
[9] Z. Li, X. Lai, S. Fu, et al., Adv. Sci. 9 (2022) 2201734.
[10] M. Zhang, S. Hu, L. Liu, et al., Signal Transduct. Target. Ther. 8 (2023) 124.
[11] H. Huang, Y. Lang, S. Wang, et al., Eng. Reg. 5 (2024) 361–374.
[12] C. Wang, R. Zhang, J. He, et al., Nat. Commun. 14 (2023) 3877.
[13] L. Amato, C. De Rosa, G. Di Guida, et al., Cell. Death. Dis. 16 (2025) 286.

[14] M. van Gulijk, A. van Krimpen, S. Schetters, et al., Sci. Immunol. 8 (2023) eabn6173.
[15] N.E. Scharping, A.V. Menk, R.D. Whetstone, et al., Cancer Immunol. Res. 5 (2017) 9–16.
[16] Q. Fu, S. Shen, P. Sun, et al., Chem. Soc. Rev. 52 (2023) 7737–7772.
[17] W. Wang, X. Zhang, R. Huang, et al., Adv. Drug Deliv. Rev. 176 (2021) 113893.
[18] X. Song, Y. Wang, C. Wang, et al., JACS 144 (2022) 10663–10687.
[19] X. Huang, T. Shen, T. Zhang, et al., AEnM 10 (2020) 1900375.
[20] Q. Liang, J. Chen, F. Wang, et al., Coordin. Chem. Rev. 424 (2020) 213488.
[21] S. Li, Y. Gao, N. Li, et al., Energy Environ. Sci. 14 (2021) 1897–1927.
[22] L. Jiao, Y. Wang, H.L. Jiang, et al., Adv. Mat. 30 (2018) 1703663.
[23] R. Huang, C.H. Li, R. Cao-Milán, et al., JACS 142 (2020) 10723–10729.
[24] C. Huang, C. Zhao, Q. Deng, et al., Nat. Catal. 6 (2023) 729–739.
[25] J. Li, X. Wang, H. Guo, et al., Chem. Eng. J. 484 (2024) 149463.
[26] G. Kroemer, C. Galassi, L. Zitvogel, et al., Nat. Immunol. 23 (2022) 487–500.
[27] J.H. Cha, W.H. Yang, W. Xia, et al., Mol. Cell. 71 (2018) 606–620 e607.
[28] G. Zhou, R. Myers, Y. Li, et al., J. Clin. Invest. 108 (2001) 1167–1174.
[29] J. Lan, L. Sun, F. Xu, et al., Cancer Res. 79 (2019) 146–158.
[30] H. Wang, W. Zhang, C. Huang, et al., Chin. Chem. Lett. 36 (2025) 111092.
[31] Z. Cui, D. Zhang, Y. Huang, et al., Chin. Chem. Lett. 36 (2025) 110460.
[32] Y. Wang, Q. Hu, Adv. Nanobiomed. Res. 3 (2023) 2200128.